nature materials

LETTERS

PUBLISHED ONLINE: 10 FEBRUARY 2013 | DOI: 10.1038/NMAT3569

Fabrication of three-dimensional electrical connections by means of directed actin self-organization

Rémi Galland[1], Patrick Leduc[2], Christophe Guérin[1], David Peyrade[3], Laurent Blanchoin[1]* and Manuel Théry[1]*

A promising approach to improve the performance of microelectronic devices is to build three-dimensional (3D) chips made of stacked circuits. However, a major hurdle lies in the fabrication of dense arrays of electrical interconnections between these layers, where accessibility is limited[1,2]. Here we show that the directed growth and self-organization of actin filaments can offer a solution to this problem. We defined the shape and orientation of 3D actin networks through both micropatterning of actin nucleation factors and biochemical control of actin filament polymerization. Networks growing from two opposing layers were able to interpenetrate and form mechanically stable connections, which were then coated with gold using a selective metallization process. The electrical conductivity, robustness and modularity of the metallized self-organized connections make this approach potentially attractive for 3D chip manufacturing.

The miniaturization and improvements in the performance of electronic devices have been mainly driven, in recent decades, by a size reduction of the components and a diversification of the fabrication technologies. However, such incremental advances reach intrinsic limits, and new technological alternatives are required for further advances. A recent and promising development is the vertical stacking of circuits to form a 3D chip[3]. Three-dimensional chips offer several important advantages over 2D circuits. A higher component density can be obtained by stacking multiple microcircuits on the footprint of a single chip. Moreover 3D integration significantly shortens the lengths of connections between different components, thus reducing signal delays and energy dissipation. Furthermore, this technology allows heterogeneous integration of various components onto a single silicon chip and thus enables the achievement of a complete functional unit in a compact volume.

A critical and challenging task in developing 3D integration at present is to build reliable and efficient electrical interconnections for signal transfer and power distribution among the stacked layers. Their fabrication is mostly limited by accessibility to the interior of the 3D chip. At present, 3D interconnections are fabricated either in between the wafers with conventional wire-bonding and direct bonding methods[2,4], or through the wafer with the 'through silicon via' approach[5,6]. Alternatively, approaches based on material self-assembly between the layers seem to show promise in the simultaneous fabrication of numerous 3D interconnections at low cost. In particular, harnessing the property of the self-organization seen in biological polymers has become an attractive solution to overcome the challenge of engineering 3D interconnections. Various types of self-organized and regular networks have been obtained from DNA (refs 7–10), amyloid fibres[11,12], genetically engineered viruses[13], peptides[14,15], microtubules[16] and actin filaments[17]. Such networks are well suited to serve as templates to form electrical wires[18–22]. However, the high precision required to control 3D network growth between two defined points on separate layers remains a major limitation in the incorporation of biological network growth into 3D chip manufacture. Actin filament networks have physical properties that largely surpass those of individual filaments owing to the presence of many different actin-binding proteins regulating the formation of various higher-order structures such as bundles or meshworks of controlled size, stiffness and orientation[23]. Here we have developed a new method based on actin filament self-organization to generate geometrically defined 3D interconnections that can be rendered electrically conductive. This method may have the potential to be used as an alternative approach for 3D chip fabrication.

We directed actin network self-organization using a micropatterning technique to define the positions of the nucleation sites for actin polymerization[17]. This technique uses deep-ultraviolet photolithography of a polyethylene glycol layer to etch out defined micropatterns competent to adsorb protein. Actin filament assembly was initiated by grafting an actin-promoting factor (the pWA domain of the WASP protein) on the micropatterned regions, and flowing an actin polymerization mix made of actin monomers and Arp2/3 complexes (Fig. 1a). This method allowed the control of the localized growth of 2D actin networks (Fig. 1b) but failed to control their 3D architecture (Fig. 1c). Indeed, actin filaments were randomly distributed all around the nucleation sites (Fig. 1b,c). We reasoned that the nucleation of a dense and reticulated network of filaments, instead of individual filaments, would constrain and thus orient network growth; and this could be performed by using actin-filament capping proteins because they have been described to promote the formation of new branches on existing filaments by blocking filament elongation[24]. This reasoning was confirmed experimentally because regular tube-like structures were formed instead of flower-like structures when capping proteins were added to the polymerization mix (Fig. 1d–f). The tube-like structures formed orthogonal to the nucleation surface and consisted of dense actin networks. The cross-sections of the tubes were consistent with

[1]Institut de Recherches en Technologies et Sciences pour le Vivant, iRTSV, Laboratoire de Physiologie Cellulaire et Végétale, CNRS/CEA/INRA/UJF, Grenoble 38054, France, [2]Laboratoire d'Electronique des Technologies de l'Information, LETI, Laboratoire d'Empilement de Circuits Avancés, CEA, Grenoble 38054, France, [3]Laboratoire des Technologies de la Microélectronique, CNRS/UJF-Grenoble1/CEA LTM, Grenoble 38054, France.
*e-mail: laurent.blanchoin@cea.fr; manuel.thery@cea.fr.

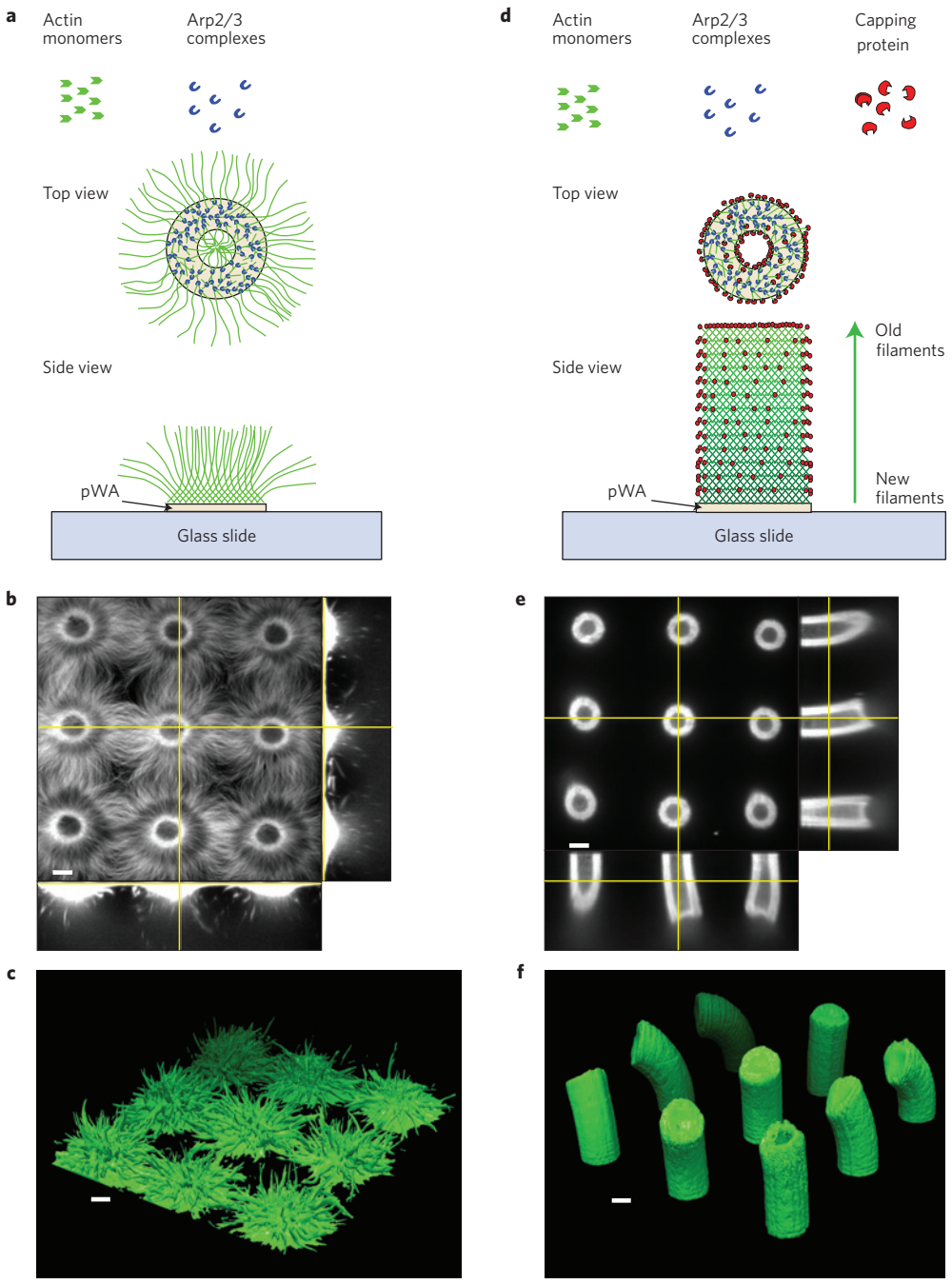

Figure 1 | Capping proteins support the oriented growth of actin networks in three dimensions. a–f, Actin network architecture on a torus-shaped micropattern in the absence (**a–c**) or presence (**d–f**) of capping proteins. **a**,**d**, Schematic representation of actin networks. **b**,**e**, Three-dimensional confocal imaging showing planar, horizontal and vertical cross-sections of actin networks polymerized on nine torus-shaped nucleating micropatterns. **c**,**f**, Three-dimensional reconstruction of the confocal images shown in **b**,**e**, respectively. Scale bars, 10 μm.

the dimensions of the micropatterned torus (Fig. 1e). Therefore, it seemed that capping proteins forced the actin network to adopt the nucleation-site geometry through promoting the addition of new filaments at the micropatterned surface. Hence, the force generated by actin filament assembly against the micropatterned surface displaced orthogonally the already assembled network. This process of actin network displacement recapitulated many of the features observed with the extensively studied actin comet propulsion of bacteria such as *Listeria monocytogenes*[25–28]. Moreover, it seemed that filament branching increased filament crosslinking and contributed to the stability of the network shape of a given cross-section as it progressively moved orthogonally and more distal to the nucleation surface (Fig. 1d). Therefore, by revising the method to include capping proteins, the shape of the actin network in 2D was, in effect, replicated as a series of layers in the third dimension.

This method could be used to generate 3D structures of various sizes and shapes by modulating the micropattern dimensions and the quantity of actin monomers. Micropatterned glass slides with arrays of 0.8- and 1.5-μm-wide dots led to the growth of 2.4- and 3-μm-high micropillars (aspect ratio of 3 and 2 respectively; Fig. 2a–c). Much larger structures could be obtained by using higher concentrations of actin monomers on larger micropatterned regions. For example, we could generate an

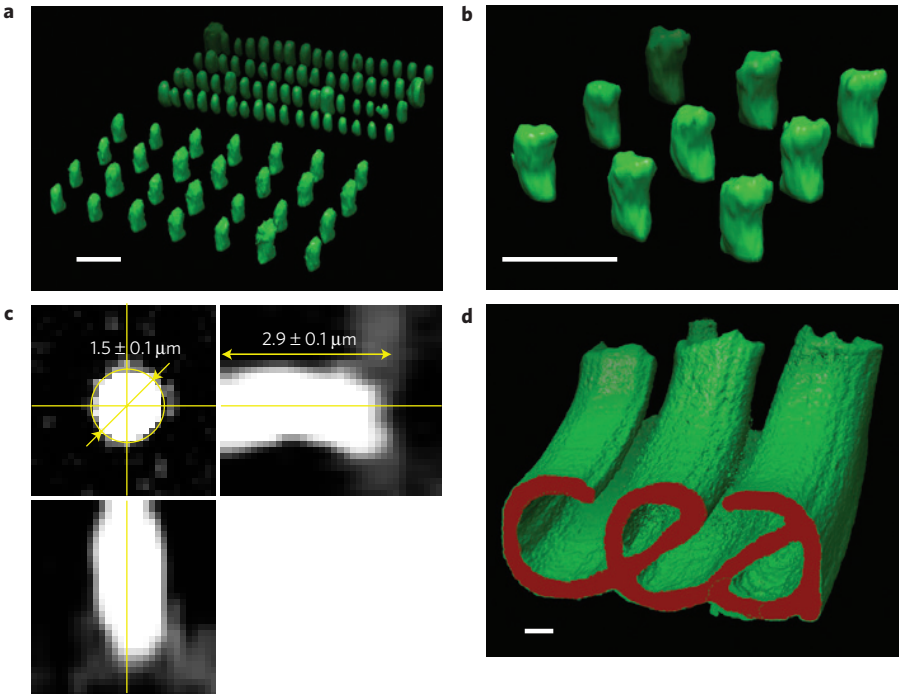

Figure 2 | The geometry of the 2D nucleation pattern dictates the size and shape of 3D actin structures. a, Three-dimensional visualization of two regular arrays of 1.5- (front) and 0.8-µm- (back) wide actin micropillars separated by 5 and 2 µm, respectively. These micropillars were generated by the vertical growth of dense actin networks out of a planar glass surface micropatterned with arrays of 0.8- and 1.5-µm-wide discs. **b**, Magnified 3D visualization of a square array of actin micropillars with a 5 µm pitch. **c**, Horizontal and vertical cross-sections of an actin micropillar showing the average dimensions measured on a dozen of such structures. **d**, Three-dimensional visualization of the large actin network (green) that has polymerized out of a CEA-shaped micropattern (red). The structure is made of 3-µm-wide vertical walls that are 36 ± 3 µm high. Scale bars, 5 µm.

18-µm-wide and 36-µm-high 3D version of our institute logo (made of 3-µm-wide walls; Fig. 2d).

We further employed this method to induce the assembly of 3D interconnections between two facing surfaces. We used laser-based micropatterning[29], which is a contact-free method, to define the nucleation sites (regular arrays of circular discs) on two opposing internal surfaces (separated by 30 µm) of a reaction chamber (Fig. 3a). The advantage of this technique was that it directly micropatterned the two surfaces without the need for an extra step to align opposing nucleation sites (Supplementary Fig. S1 and Methods). Introducing the actin polymerization mix resulted in the growth of 10-µm-wide cylinders that collided midway between the two opposing surfaces (Fig. 3b,c). The quantity of actin monomers in the polymerization mix per structure affected whether and how links were formed. Using a polymerization mix with 2 µM of actin monomers in 2.25 µl to generate two arrays of 9 × 9 cylinders, a total amount of 55 fmol of actin was attributed to each structure. This quantity allowed the two cylinders to grow up to 16 µm in length and make contact with a minimum of deformation (Fig. 3d). Below this quantity of actin monomers, the two cylinders failed to make contact. Higher quantities of actin monomers induced a deformation of the two cylinders on contact (Supplementary Fig. S2A), such that the actin polymerization at the surface of the micropatterned sites forced the two contacting cylinders to bend irreversibly (Supplementary Fig. S2A). The dimensions of the structure also affected whether and how links were formed. Below 5-µm-wide diameters, cylinders could not grow orthogonally up to 15 µm without deforming (Supplementary Fig. S2B). Cylinders 20-µm-wide grew orthogonally up to 15 µm, but the force induced by actin polymerization induced the cylinders to fracture (Supplementary Fig. S2B,C). Other nucleation-site geometries with similar large widths also induced fractures. Therefore, the alteration of nucleation-site geometries alone was not sufficient to prevent structure deformation on contact. Rather, the quantity of actin monomer had to be precisely controlled to induce mechanically stable links.

To overcome this limitation, we explored generating structures that could give rise to a plug-and-socket-like connection, and therefore selected a circular disc and a torus as two opposing nucleation-site geometries (Fig. 3e). With a 30 µm-separation distance in the chamber, 7.5-µm-diameter cylinders from circular nucleation sites (that is plugs) were up to 20 µm in length and entered up to 3 µm into the lumens of opposing tubes (that is, sockets), which had inner diameters of 12 µm and were 13 µm in length from the torus nucleation sites (Fig. 3f–h). Again, the quantity of actin monomers per connection and the geometry of the structures affected whether and how the connections formed (Supplementary Fig. S3). Less than 40 fmol of actin monomers per connection failed to generate cylinders and tubes of a sufficient length to make contact (Supplementary Fig. S3A); and more than 100 fmol per connection generated overly-long structures that were deformed by the mutual contact (Supplementary Fig. S3A). Moreover, the maximum distance a cylinder could enter into an opposing tube was 5 µm. A quantity of actin monomers per connection between 50 and 100 fmol was optimal to achieve efficient and stable connections. The 5-µm-long penetration depth offered a wider tolerance for actin quantities compared with collision-based links. Cylinders less than 5 µm in diameter did not grow orthogonally up to 15 µm without deforming (Supplementary Fig. S3C). Tubes made of sheets thinner than 2.5 µm could not resist the force generated by the growing cylinder and failed to create connections (Supplementary Fig. S3D). For cylinders 5 µm or more in diameter, a ratio close to 0.6–0.7 between the cylinder diameter and the tube inner diameter was necessary to obtain efficient and reproducible plug-and-socket connections (Fig. 3g,h and Supplementary Fig. S3B). Therefore, this confirms that by identifying the appropriate

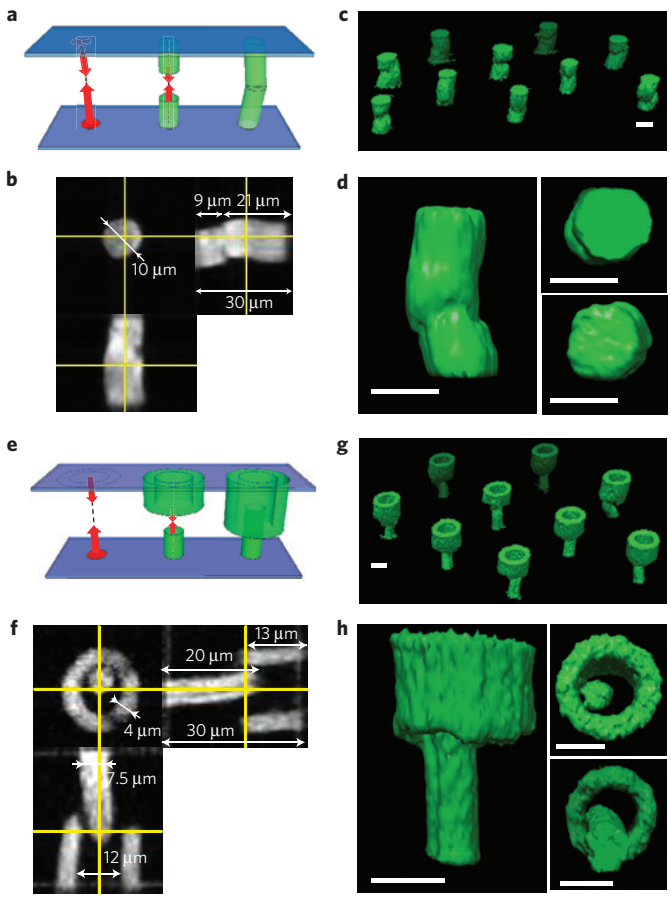

Figure 3 | Actin network growth from two opposing surfaces induces the formation of 3D interconnections. a, Schematic representation of 3D links formed by collision of two actin structures growing from opposing surfaces. Arrows represent network growth. **b**, Three-dimensional visualization showing horizontal and vertical cross-sections of an actin network polymerized between two circular-shaped micropatterns. **c**, Three-dimensional visualization of a regular array of 3D actin links separated by 60 µm. Cylinders are 7.5 µm wide in the right two diagonals and 10 µm wide in the left two diagonals. **d**, Three-dimensional visualization of the images shown in **b**. **e**, Schematic representation of 3D connections formed by a cylinder entering into the lumen of a hollow tube. Arrows represent network growth. **f**, Three-dimensional visualization showing horizontal and vertical cross-sections of actin structures polymerized from opposing surfaces with discoidal- and torus-shaped nucleation sites, leading to the growth of a cylinder and hollow tube, respectively. **g**, Three-dimensional visualization of a regular array of connecting actin structures from two opposing surfaces separated by 60 µm. **h**, Three-dimensional visualization of the images shown in **f**. Scale bars, 10 µm.

biochemical and geometrical parameters, this method can be used to build robust 3D interconnections between two surfaces based on the self-organization of growing actin networks.

The application of this method to the manufacture of 3D electronic chips would require the conversion of self-organized and organic connections between layers into conductive wires. On the basis of previous work[19,30], we have adapted an electroless metallization technique to coat dense actin networks with a layer of gold (Fig. 4).

First, the bio-templates were decorated with metallic clusters. Present methods are based on the attachment of functionalized metallic nanoparticles onto the bio-templates either through already existing reactive moieties[19,20,22] or through reactive moieties added by genetic engineering[13,31]. These metallic clusters can further serve as seeds for a metallic plating step to enlarge them and create a continuous metallic coating on the bio-templates[13,19,20,22,31]. In our case, the actin interconnections were first fixed with glutaraldehyde, a crosslinking agent, to rigidify the network and allow it to resist the fluid flow and the biochemical conditions during metallization (Fig. 4a). Mono-maleimide gold nanoparticles were then attached to the actin interconnections through reaction with the thiol group found on the cysteine of actin molecules. A patented metallization solution, GoldEnhance, containing gold ions and a reducing agent, was finally used to enlarge the metallic seeds up to the formation of a conductive gold layer on the actin network (Fig. 4a). This technique was applied to the metallization of 3D actin links. The mechanical resistance of the links before the glutaraldehyde fixation step was improved by adding α-actinin, an actin-filament crosslinking protein, to the polymerization mix. A 3D reconstruction of the gold coating visualized in reflection microscopy showed that the structures were sufficiently strong to resist all fluid exchanges and the harsh chemical conditions during metallization (Fig. 4b).

The electrical properties of metallized dense actin networks were characterized using a two-point measurement technique. A 100-µm-long metallized-actin meshwork assembled on a planar surface was easy to access to with the two electrodes (Fig. 4c). The chemical composition analysis with energy-dispersive X-ray spectroscopy (EDS) and the observation of the metallized actin meshwork with scanning electron microscopy revealed the presence of large aggregates corresponding to salt precipitates and smaller clusters corresponding to the gold-coated particles (Fig. 4c). The electrical measurement method consisted of measuring the current through the electrodes in contact with the actin network (Fig. 4c). Although no current was measured when the electrodes were in contact with the surface next to the metallized actin meshwork, currents of a few microamperes could be measured in the network in response to a few volts (Fig. 4d). We observed linear I–V curves, evidence of an ohmic conduction, with resistance ranging from 5×10^8 to 4×10^9 Ω (Supplementary Fig. S4) depending on the metallization batch and the structure measured. This variability was probably due to structural defects in the fixed network and limited efficacy of the metallization process. This method leaves room for improvement on these two steps. These results nevertheless demonstrate that the dense metallized actin networks were conductive.

This work paves the way towards the use of self-organized biological structures in the manufacturing of interconnections between stacked layers in 3D electronic chips. The precise control over the growth and shape of the actin network with simple micropatterning techniques and biochemically defined actin polymerization provides a robust method to form numerous interconnections between two surfaces. Only a limited number of proteins have been examined in this study to regulate network architecture and the mechanical strength of the interconnections. However, there are numerous types of protein that modulate different aspects of cell-cytoskeleton self-organization, and they constitute a wide range of tools, which could be used to modulate the structure and the dynamics of networks to offer further control over interconnection assembly. Therefore, the robustness, versatility and modularity of an assembly process based on biological self-organization, such as the one described here, may find a broad range of applications and have a promising future in the manufacture of micro- and nano-devices.

Methods

Deep ultraviolet micropatterning. Glass coverslip micropatterning has been described elsewhere[32]. Coverslips were first spin-coated for 30 s at 1,000 r.p.m. with adhesion promoter TI-Prime (MicroChemicals), backed for 5 min at 120 °C and then spin-coated with 1% polystyrene (SIGMA) in toluene (SIGMA) at 1,000 r.p.m. for 30 s. Polystyrene-coated coverslips were oxidized with oxygen plasma treatment (FEMTO, Diener Electronics) for 30 s at 60 W before incubating with 0.1 mg ml^{-1}

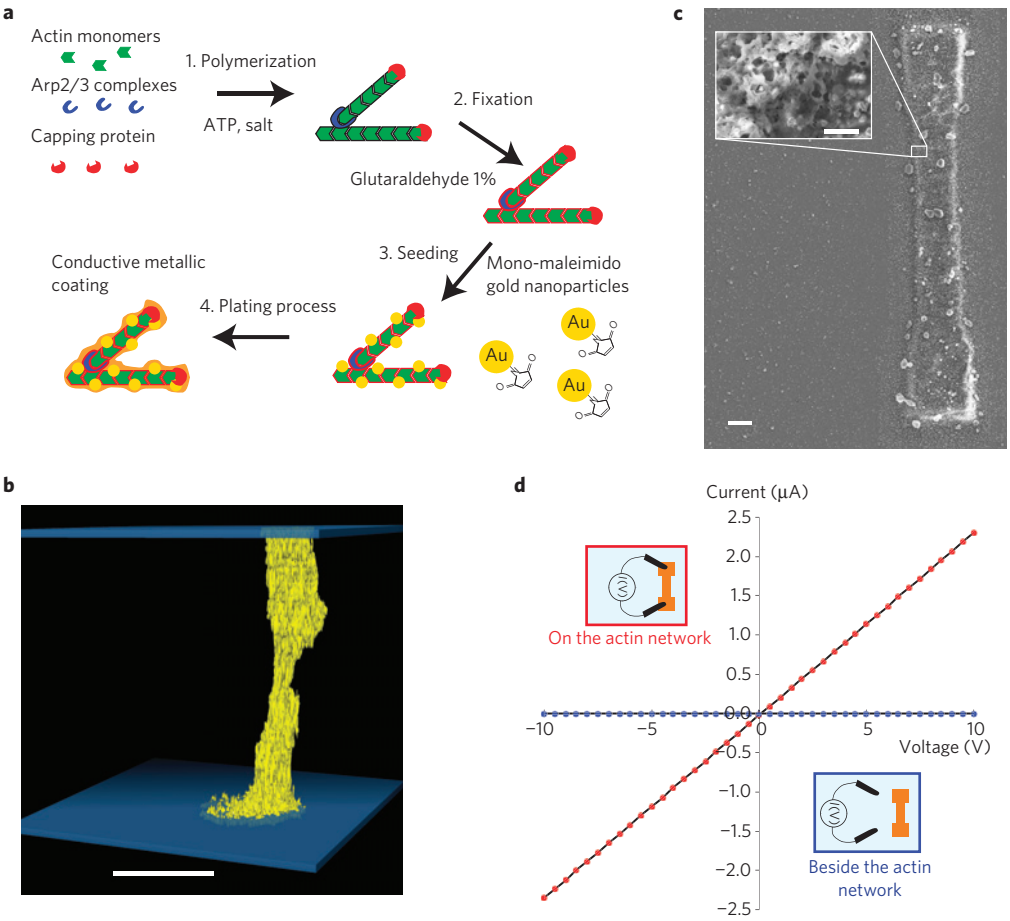

Figure 4 | Metallization of actin filaments ensures network electrical conductivity. a, Schematic representation of the selective metallization process. **b**, 3D visualization of a 3D metallized actin link. Reflection microscopy revealed the reflected light on metallic particles (yellow); the opposing surfaces (glass slides) are represented in blue. **c**, SEM image of a metallized planar actin network that was used for conductivity measurements. The inset shows a magnification of the interconnected gold aggregates. **d**, Electrical characterization of metallized planar actin networks. The current intensity was measured for various voltage tensions applied on the networks (red). Control measurements were performed adjacent to the metallized planar actin networks (blue). See Supplementary Fig. S4 for more measurements. Scale bars, 10 μm in **b**,**c** and 1 μm in the inset.

poly(L-lysine)–poly(ethylene glycol) (JenKem Technology) in 10 mM HEPES at pH 7.4 for 30 min. After drying, pegylated coverslips were exposed to deep ultraviolet (UVO cleaner, Jelight) through a photomask (TOPPAN) for 5 min.

To graft the nucleation-promoting factor pWA on the ultraviolet-exposed coverslips, they were mounted on a pegylated glass slide with calibrated spacers of 180 μm (LIMA) to define a reaction chamber. The reaction chamber was filled with a solution of pWA at 1 μMfor 15 min and then rinsed with 10× KMEI buffer (500 mM KCl, 10 mM $MgCl_2$, 10 mM EGTA and 100 mM imidazole at pH 7.8) diluted ten times in a G-actin buffer (2 mM Tris-Cl, 0.2 mM ATP, 0.5 mM dithiothreitol, 0.1 mM $CaCl_2$ and 1 mM Na azide). The reaction chamber was then stored at 4 °C before use.

Laser micropatterning. Laser patterning has been described elsewhere[29]. Laser patterning was performed using the iLasPulse device (Roper Scientific) set up on an inverted microscope (TE2000-E, Nikon). iLasPulse is a dual-axis galvanometer-based optical scanner that focalizes the laser beam on the sample (diffraction-limited spot size) on the whole field of view of the camera. It includes a telescope to adjust laser focalization with image focalization and a polarizer to control beam power. The laser used is a passively Q-switched laser (STV-E, TeamPhotonics) that produces 300 ps pulses at 355 nm (energy per pulse 1.2 μJ, peak power 4 kW, variable repetition rate 0.01–2 kHz, average power $\leq$ 2.4 mW). Laser displacement, exposure time and repetition rate are controlled using Metamorph software (Universal Imaging Corporation). The objective used is a CFI S-Fluor oil ×100/1.3 objective (Nikon). The laser was scanned throughout the area of interest with 300 nJ pulses (set with the polarizer).

Before the laser patterning, two pegylated coverslips were mounted together with calibrated spacers of 30 μm (LIMA) to define a size-controlled reaction chamber of 2.25 μl (30 μm × 15 mm × 5 mm). The reaction chamber was then filled with a solution of the nucleation-promoting factor pWA at 1 μM, which was adsorbed onto the laser-patterned regions. On the bottom surface of the reaction chamber, each spot was exposed for 5 ms at a repetition rate of 2,000 Hz. On the upper surface of the reaction chamber, each spot was exposed for 8 ms at a repetition rate of 2,000 Hz. After patterning, the reaction chamber was rinsed with KMEI buffer and stored at 4 °C before its use.

Actin polymerization. Protein mixtures were diluted in freshly prepared X buffer (10 mM HEPES, pH 7.4, 0.1 M KCl, 1 mM $MgCl_2$, 1 mM ATP and 0.1 mM $CaCl_2$) supplemented with 1% BSA, 0.2% methylcellulose, 3 mM dithiothreitol, 0.13 mM DABCO and 1.8 mM ATP. Actin polymerization without capping protein was induced in a solution containing 3 μM actin monomers (10% labelled with Alexa 568), 9 μM profilin, 2 μM phalloidin and 50 nM Arp2/3 complex. Actin polymerization with capping protein was induced in a solution containing between 1.5 and 4.5 μM actin monomers (10% labelled with Alexa 568), three equivalents of profilin, 2 μM phalloidin, 50 nM Arp2/3 complex and 60 nm capping protein.

Electroless metallization. Actin structures were fixed 1 h after polymerization, with a solution of glutaraldehyde at 1% diluted in KMEI buffer for 20 min and then rinsed with ultrapure water. The structures were then incubated overnight at 4 °C with a solution of Mono-Maleimido Nanogold particles (Nanoprobes) diluted in 50 mM of NaPI buffer (pH 7.4). The electroless metallization process was then performed with a GoldEnhance LM kit (Nanoprobes). A first incubation step was done in GoldEnhance solution diluted five times in His buffer for 1 h. After rinsing with ultrapure water, a second incubation step was performed with GoldEnhance solution diluted twice for 20 min. A final incubation step was then performed with non-diluted GoldEnhance solution for 7 min. The structures were then rinsed with ultrapure water and were allowed to dry in air.

Microscopy and scanning electron microscopy imaging. Confocal acquisition was performed on an Eclipse TI-E Nikon inverted microscope equipped with a CSUX1-A1 Yokogawa confocal head and an Evolve EMCCD camera

(Ropert Scientific—Princeton Instrument). A CFI Plan APO VC oil ×60/1.4 objective or a CFI Plan Fluor oil ×40/1.3 objective (Nikon) was used. The system was driven by Metamorph software (Universal Imaging Corporation).

Confocal image analyses were performed with ImageJ (http://rsb.info.nih.gov/ij). The images were first filtered to remove the acquisition noise with a dedicated plugin. The images were then deconvolved with the Iterative Deconvolve 3D plugin to take into account the optical aberrations of our microscopy set-up.

Three-dimensional reconstructions were performed with the UCSF Chimera package. Chimera is developed by the Resource for Biocomputing, Visualization, and Informatics at the University of California (San Francisco) with support from the National Institutes of Health (National Center for Research Resources grant 2P41RR001081, National Institute of General Medical Sciences grant 9P41GM103311).

Scanning electron microscopy (SEM) imaging was performed on a Zeiss Ultra *plus* SEM system (Carl Zeiss SMT) equipped with an XFlash detector 5030 (Bruker) for EDS. The analysis of EDS data was carried out using the EDS Bruker software ESPRIT. To perform SEM analysis we created the metallized actin networks on ITO-coated coverslips (Diamond Coating) using the deep ultraviolet patterning method described above.

Conductivity characterization. Conductivity characterization of 2D metallized actin networks was performed on a Cascade Microtech S300 probe station (Cascade Microtech). The electrical measurements were carried out using a DCM-210 Precision Positioner (Cascade Microtech) to position two probes on each extremity of a 200-μm-long metallized actin network. The I–V curve measurements on and adjacent to the metallized actin networks were performed between −10 and 10 V every 1 V using a 4156C Precision Semiconductor Parameter Analyzer (Agilent).

Received 14 August 2012; accepted 9 January 2013; published online 10 February 2013

References

1. Farooq, M. G. & Iyer, S. S. 3D integration review. *Sci. China Inform. Sci.* **54,** 1012–1025 (2011).
2. Garrou, P., Bower, C. & Ramm, P. *Handbook of 3D Integration: Technology and Applications of 3D Integrated Circuits* (Wiley, 2008).
3. Emma, P. G. & Kursun, E. Is 3D chip technology the next growth engine for performance improvement? *IBM J. Res. Dev.* **52,** 541–552 (2008).
4. Cale, T. S., Lu, J-Q. & Gutmann, R. J. Three-dimensional integration in microelectronics: Motivation, processing, and thermo mechanical modeling. *Chem. Eng. Commun.* **195,** 847–888 (2008).
5. Leduc, P. *et al. 2009 IEEE Int. Conf. on 3D System Integration* 1–5 (IEEE, 2009).
6. Jourdain, A. *et al. IEEE 61st Electronic Components and Technology Conf.* 1122–1125 (IEEE, 2011).
7. Winfree, E., Liu, F., Wenzler, L. A. & Seeman, N. C. Design and self-assembly of two-dimensional DNA crystals. *Nature* **394,** 539–544 (1998).
8. Rothemund, P. W. K. Folding DNA to create nanoscale shapes and patterns. *Nature* **440,** 297–302 (2006).
9. Douglas, S. M. *et al.* Self-assembly of DNA into nanoscale three-dimensional shapes. *Nature* **459,** 414–418 (2009).
10. Han, D. *et al.* DNA origami with complex curvatures in three-dimensional space. *Science* **332,** 342–346 (2011).
11. Dinca, V. *et al.* Directed three-dimensional patterning of self-assembled peptide fibrils. *Nano Lett.* **8,** 538–543 (2008).
12. Adler-Abramovich, L. *et al.* Thermal and chemical stability of diphenylalanine peptide nanotubes: Implications for nanotechnological applications. *Langmuir* **22,** 1313–1320 (2006).
13. Huang, Y. *et al.* Programmable assembly of nanoarchitectures using genetically engineered viruses. *Nano Lett.* **5,** 1429–1434 (2005).
14. Scanlon, S. & Aggeli, A. Self-assembling peptide nanotubes. *Nano Today* **3,** 22–30 (June–August, 2008).
15. Zhang, S. Fabrication of novel biomaterials through molecular self-assembly. *Nature Biotechnol.* **21,** 1171–1178 (2003).
16. Portran, D., Gaillard, J., Vantard, M. & Thery, M. Quantification of MAP and molecular motor activities on geometrically controlled microtubule networks. *Cytoskeleton* **70,** 12–23 (2013).
17. Reymann, A-C. *et al.* Nucleation geometry governs ordered actin networks structures. *Nature Mater.* **9,** 827–832 (2010).
18. Gazit, E. Use of biomolecular templates for the fabrication of metal nanowires. *FEBS J.* **274,** 317–322 (2007).
19. Patolsky, F., Weizmann, Y. & Willner, I. Actin-based metallic nanowires as bio-nanotransporters. *Nature Mater.* **3,** 692–695 (2004).
20. Zhou, J. C. *et al.* Microtubule-based gold nanowires and nanowire arrays. *Small* **4,** 1507–1515 (2008).
21. Braun, E., Eichen, Y., Sivan, U. & Ben-Yoseph, G. DNA-templated assembly and electrode attachment of a conducting silver wire. *Nature* **391,** 775–778 (1998).
22. Pearson, A. C. *et al.* DNA origami metallized site specifically to form electrically conductive nanowires. *J. Phys. Chem. B* **116,** 10551–10560 (2012).
23. Michelot, A. & Drubin, D. G. Building distinct actin filament networks in a common cytoplasm. *Curr. Biol.* **21,** R560–R569 (2011).
24. Blanchoin, L. *et al.* Direct observation of dendritic actin filament networks nucleated by Arp2/3 complex and WASP/Scar proteins. *Nature* **171,** 1007–1011 (2000).
25. Loisel, T. P., Boujemaa, R., Pantaloni, D. & Carlier, M. F. Reconstitution of actin-based motility of *Listeria* and *Shigella* using pure proteins. *Nature* **401,** 613–616 (1999).
26. Oudenaarden, A. Van & Theriot, J. A. Cooperative symmetry-breaking by actin polymerization in a model for cell motility. *Nature Cell Biol.* 493–499 (1999).
27. Van der Gucht, J., Paluch, E., Plastino, J. & Sykes, C. Stress release drives symmetry breaking for actin-based movement. *Proc. Natl Acad. Sci. USA* **102,** 7847–7852 (2005).
28. Achard, V. *et al.* A 'primer'-based mechanism underlies branched actin filament network formation and motility. *Curr. Biol.* **20,** 423–428 (2010).
29. Vignaud, T. *et al.* Reprogramming cell shape with laser nano-patterning. *J. Cell Sci.* **125,** 2134–2140 (2012).
30. Behrens, S., Habicht, W., Wagner, K. & Unger, E. Assembly of nanoparticle ring structures based on protein templates. *Adv. Mater.* **18,** 284–289 (2006).
31. Scheibel, T. *et al.* Conducting nanowires built by controlled self-assembly of amyloid fibres and selective metal deposition. *Proc. Natl Acad. Sci. USA* **100,** 4527–4532 (2003).
32. Azioune, A., Carpi, N., Tseng, Q., Théry, M. & Piel, M. Protein micropatterns: A direct printing protocol using deep UVs. *Methods Cell Biol.* **97,** 133–146 (2010).

Acknowledgements

This work was supported by the 'Chimtronique' programme of the CEA. It has been performed with the help of the 'Plateforme technologique amont' of Grenoble, and with the financial support of the 'Nanosciences aux limites de la Nanoélectronique' Foundation. We thank J-C. Gabriel for constructive discussions, F. Perraut for technological advice and C. Suarez for his support in biochemistry.

Author contributions

R.G., C.G. and P.L. carried out the experiments. D.P., L.B. and M.T. directed the project. R.G., L.B. and M.T. wrote the manuscript.

Additional information

Supplementary information is available in the online version of the paper. Reprints and permissions information is available online at www.nature.com/reprints. Correspondence and requests for materials should be addressed to L.B. or M.T.

Competing financial interests

The CEA and the CNRS have filed an application for a patent on the technology described in this manuscript, of which R.G., L.B. and M.T. are inventors.